Plasma Chem Plasma Process (2016) 36:29–44
DOI 10.1007/s11090-015-9654-5

REVIEW ARTICLE

A Short Review of Experimental and Computational Diagnostics for Radiofrequency Plasma Micro-thrusters

C. Charles[1] · A. Bish[1] · R. W. Boswell[1] · J. Dedrick[1] · A. Greig[1] · R. Hawkins[1] · T. S. Ho[1]

Received: 15 June 2015 / Accepted: 22 August 2015 / Published online: 10 September 2015

Abstract Experimental and computational diagnostics for radiofrequency plasma micro-thrusters are presented, based on the low power (10–100 W) electrothermal thruster prototype, *Mini Pocket Rocket*, developed for use on the *Cubesat* nanosatellite platform. Computer simulations include computer fluid dynamics simulations and particle in cell simulations while experimental results are obtained using a variety of electrostatic, optical and momentum probes. The output and limitations of each diagnostic are discussed within the context of device development for space use.

Keywords Micro-thruster · Radiofrequency · Diagnostics · Plasma

Introduction

A large number of electric propulsion systems are presently operational on satellites: these include resisto-jets, gridded ion beam and Hall effect thrusters, the latter two requiring hollow cathode neutralisers [1]. The propellant choice ranges from inert gases such as non-reactive xenon through molecular gases to highly reactive chemicals such hydrazine. The path from laboratory to space is long, costly and risky and includes basic plasma research, propulsion system development and testing, space qualification, space launch and mission control. It necessitates dedicated infrastructure for space qualifications on Earth. Launch into space is very challenging for small university groups who commonly cannot afford regulations and policy compliance. However, new opportunities are emerging with the development of *Cubesat* nanosatellites (1 Unit defined as 10 cm × 10 cm × 10 cm at about 1 kg), *Cubesat* arrays (6 Units at about 6 kg) and small satellites (30–50 kg) which are ideal host for technology demonstrator payload. The *Cubesat* platform offers a low-cost

✉ C. Charles
christine.charles@anu.edu.au

[1] Space Plasma, Power and Propulsion Laboratory, Research School of Physics and Engineering, The Australian National University, Canberra, ACT 2601, Australia

effective path to space and is well suited to the development and testing of small plasma jets in small size vacuum chambers usually available in research laboratories.

The broad range of plasma excitation frequencies have been employed for space thrusters; for example the ion gridded thruster has been developed using either direct current (i.e. *Kaufman* thruster), radiofrequency (i.e. *RIT* thruster) or microwave (i.e. *Hayabusa* 1 and 2) excitation systems [1]. Their high performance characteristics result from the separation of plasma generation and ion acceleration so that for high current, high voltage systems the power for ion acceleration far exceeds the power necessary for plasma generation. Nevertheless, they require electrode grids immersed in the plasma to extract and accelerate ions and these ions need to be neutralised by electrons produced by a separate Hollow Cathode-type plasma generator to allow for plasma plume detachment and thrust generation. These neutralizing systems add another level of complexity to the thruster and require a separate power supply and gas control.

Since small size ($\sim$ mm diameter) collisional plasma jets have already been applied to a variety of research fields (i.e. materials processing [2], plasma medicine [3], Hollow Cathode neutralisers for space use [1]), their possible use as a micro-propulsion system to assist with orbit boosting and attitude control of micro-satellites is under investigation. The presence of neutral gas heating within the plasma jet could provide added momentum and a better fuel efficiency compared to cold gas thrusters. Here the main experimental and computational diagnostics developed for the study of plasma jets are presented, based around the current development at the Australian National University of the *Mini Pocket Rocket* electrothermal radiofrequency thruster.

Experimental Radiofrequency Plasma Jet Prototype

The radiofrequency (rf at 13.56 MHz) electrothermal plasma micro-thruster called *Mini Pocket Rocket (MiniPR)* is a small compact thruster prototype with a cylindrical ceramic plasma cavity of 1.8 mm in length and 1.5 mm in diameter surrounded by a central annular 5 mm-wide rf copper electrode fed by the 13.56 MHz power via an impedance matching network and two grounded 3 mm-wide aluminium electrodes separated by two ceramic rings (Fig. 1). Here it is mounted onto the previously described 1 metre-long 1 metre-diameter *Irukandji* vacuum chamber equipped with a turbo/primary pumping system, an ion gauge and a convectron gauge [4, 5] and achieving a base pressure of about 7×10^{-7} Torr (Fig. 1). Propellant gas (typically argon or xenon) is introduced via a 4 cm-diam 1.6 cm-long cavity, the plenum (equipped with a viewing window), flows through *MiniPR*'s plasma cavity and expands into the vacuum chamber. A gas flow of about 15 sccm (0.45 mg s^{-1}) yields a plenum pressure of 1.6 Torr and a chamber pressure of 2.5×10^{-4} Torr, hence an upstream to downstream pressure ratio of about 6700.

The plasma is employed to heat the gas via charge exchange collisions and ambipolar flow to create a form of electrothermal thruster which has its heating mechanism in the centre of the flowing propellant as well as on the thermally lossy walls. It is a low-volume, low-cost, low-weight, rf plasma thruster which can operated with green and safe propellants, typically argon. It can easily be operated as a cold gas thruster. The capacitively coupled rf generates a high density plasma at a few Torrs having a volume less than 1 millilitre that serves as an intermediary in the power flow but is not directly involved in producing thrust. Two effects having distinct time-scale contribute to neutral heating: ambipolar diffusion heats the neutrals via ion-neutral collisions (microsecond time scale)

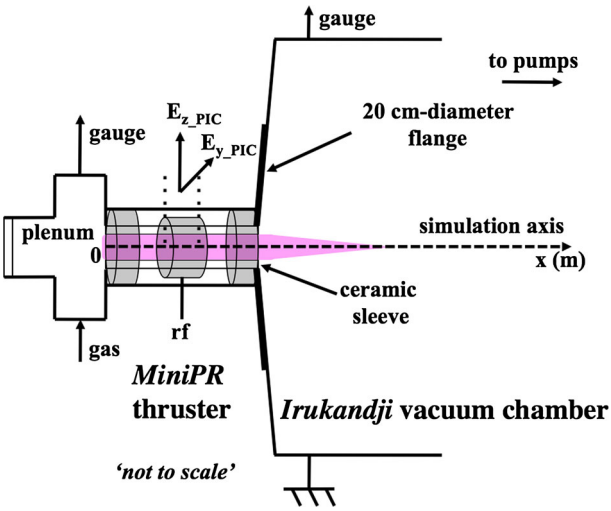

Fig. 1 Schematic of the experimental set up showing the *MiniPR* radiofrequency plasma thruster mounted within a vacuum flange attached to the larger *Irukandji* vacuum chamber

and radial wall heating resulting from ion neutralisation heats the neutrals on a time scale of tens of seconds [6].

Two distinct impedance matching systems can be used to couple rf power into *MiniPR*: the first system is a 'traditionally' used Π matching network (within a copper box $0.15 \times 0.4 \times 0.4$ m in size) equipped with two variable vacuum capacitors, two fixed capacitors and an inductor [4]. The second impedance matching system consists of a compact low-weight (90 g) small-volume fixed ceramic capacitor and one inductor assembly mounted on a printed circuit board (PCB). This variable frequency matching rf tuning system is suited to space use. The power and voltage limitations are related to the size and heat transfer capability of the PCB. A standard format for the *Cubesat* platform is PC104.

Electrical Diagnostics

For such a capacitively coupled plasma discharge, a commercially available *Octiv Impedans IV* probe typically inserted between the matching network and the discharge gives access to the rf plasma current, voltage, phase and delivered rf power. The use of the *Advanced Energy Paramount 3013* rf generator with a 12.882 MHz to 14.238 MHz frequency range also provides real time measurements of load impedance $Z = R + jX$, delivered power and standing wave ratio. The minimum plasma cavity diameter size which would allow the use of an electrostatic probe such as a Langmuir probe would be about 4 mm and such measurements of plasma density and electron temperature have been obtained in two other similar devices [7, 8]. The measured axial density profile of [7] is shown by open circles on Fig. 2. These measurements help validating computer simulations [9]. Here such Computer Fluid Dynamics (CFD) simulations are used to study the effect of a pressure gradient similar to that existing for the prototype shown on Fig. 1 as described in Sect. 8.

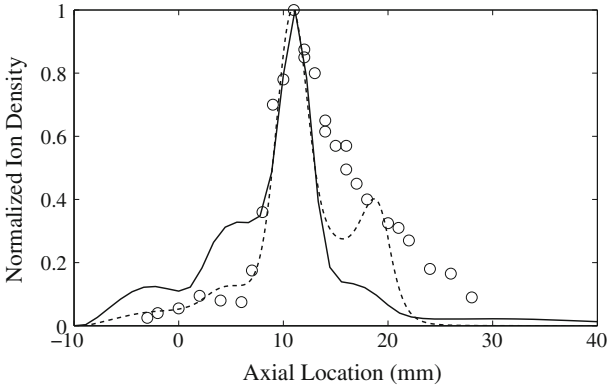

Fig. 2 Normalized ion saturation current along the central axis measured using a Langmuir Probe (*open circles*) [7], simulated ion density along the central axis with a pressure gradient of two (*solid line*) and simulation ion density along the central axis with a pressure gradient of 2000 (*dashed line*)

Optical Diagnostics

Non-invasive optical emission spectroscopy (OES) diagnostics are a powerful tool for analysing plasma discharges. They vary from simple light intensity measurement using a photodiode to more advanced optical diagnostics aiming at determining parameters such as electron density and temperature, absolute densities and radical concentrations [10]. Of particular interest here are temperature measurements and electron behaviour, which can be respectively investigated through rovibrational spectroscopy and nanosecond imaging as outlined below.

Rovibrational Spectroscopy

Theoretical calculations show that a few 10 s of Watts input power in the plasma results in gas temperature of 1000–2000 K [7]. This is verified experimentally by rovibrational spectroscopy. Rovibrational spectroscopy focusses on the study of diatomic or molecular species with excited rotational and vibrational states. Rotational and vibrational states within a molecule add additional excitation channels for electrons, and the resulting spectra are quite different from that of an atomic element.

For an atomic element, the difference in electron energy levels depends mainly on the electronic state of the atom, resulting in a spectrum of sharp narrow peaks. A molecular species has multiple rotational modes and one or more vibrational modes, so within an electronic transition the electron may move between differing vibrational states, identified by vibrational quantum number (v), and rotational states, identified by rotational quantum number (J). There is no longer a single well defined energy difference and the resulting spectra consist of a series of rovibrational bands rather than single sharp peaks.

The relative intensities of the vibrational and rotational bands are dependant on the distribution of particles within the vibrational and rotational states, and hence the vibrational temperature (T_v) and rotational temperature (T_r). Additionally, for certain rovibrational bands, the intensity profile of the band can be simulated using well published equations and constants. Therefore estimates for T_v and T_r of an experimental discharge can be found using rovibrational spectroscopy band fitting, by iteratively comparing experimentally recorded spectra with simulated spectra of known T_r and T_v until a good fit is found. The temperatures used in the fitted simulated spectra are then approximately T_r and T_v of the experimental discharge [11].

Under certain conditions, T_r and the gas temperature (T_g) can be assumed to be in equilibrium. For this to occur, the lifetime of the ground rotational state must be longer than the time between collisions [12] allowing for molecules in the rotational ground state to thermalise. Additionally, as the light analysed is due to emission from an upper rotational state, not the ground state, it is also a requirement that the upper and ground rotational states have similar distributions. This can be safely assumed if the upper state is populated mostly through electron impact excitation collisions. Electrons having low mass do not significantly alter the molecular rotational moment during a collision and the ground states effectively maps onto the upper state [13]. Finally, the lifetime of the excited state must be shorter than the time between heavy particle collisions, such that the rotational distribution is not altered from that of the ground state.

Rovibrational spectroscopy has been previously used to determine the temperature of discharges ranging from atmospheric pressure [14] to around a Torr [15] using a range of gases including O_2 [16], C_2 [15] and N_2 [17]. Addition of trace amounts of a diatomic gas to an atomic element discharge allows for the same rovibrational spectroscopy method described above to be used to estimate the gas temperature of an atomic discharge [13, 15, 18].

Here, the temperature of an argon discharge with 1 % N_2 added is estimated using the N_2 SPS (Second Positive System) in the wavelength range 372 nm to 381 nm encompassing the (0,2) and (1,3) bands. Addition of trace amounts of N_2 to an argon plasma may alter the discharge properties, especially in regards to opening up new excitation channels for the SPS from resonant energy transfer between argon metastable atoms and N_2 molecules [19]. This can lead to overestimation of gas temperatures found using rovibrational band matching [13]. However, the temperature of a 1.5 Torr, 10 W argon with 1 % N_2 plasma was recently found to correspond to the theoretical gas temperature of a pure argon discharge calculated using an analytic model of ion-neutral charge exchange collisions [20], giving confidence that any changes to the discharge properties or rovibrational band matching are minimal.

Generation of the simulated spectra is achieved by calculating the wavelength of the required transition lines and the related intensities, then broadening the lines to match the experimentally determined spectra [11]. The wavelength (λ) of an electronic transition from the $Cv'J'$ to $Bv''J''$ state is

$$\lambda_{Bv'',J''}^{Cv',J'} = \left[n_a \sum_{pq} Y_{pq}^{C} \left(v' + \frac{1}{2} \right)^p [J'(J'+1)]^q - Y_{pq}^{B} \left(v'' + \frac{1}{2} \right)^p [J''(J''+1)]^q \right]^{-1} \quad (1)$$

where n_a is the refractive index of air. The constants Y_{pq} are Dunham coefficients [21] with subscripts p and q referring to the powers of the vibrational and rotational quantum numbers, respectively. These were taken from Bai et al. [15] for values of p from 0 to 5 and q from 0 to 2. For each wavelength calculated, the intensity (I) of the spectrum is determined using

$$I_{Bv'',J''}^{Cv',J'} = \frac{D}{\lambda^4} q_{v',v''} e^{\frac{-E_{v'}}{kT_v}} S_{J',J''} e^{\frac{-E_{J'}}{kT_r}} \quad (2)$$

where D is an arbitrary scaling constant, k is Boltzmann's constant, $q_{v',v''}$ are Franck-Condon factors (taken from Zare *et al.* [22]) and $S_{J',J''}$ are Holn-London factors calculated from Herzberg [23] (pg 208). The rotational energy ($E_{J'}$) and vibrational energy ($E_{v'}$) are

given by [23] $E_{J'} = hcB_{v'}J'(J'+1) + hcD_{v'}J'(J'+1)^2$ and $E_{v'} = hc\omega_e(v'+\frac{1}{2}) - hc\omega_e x_e(v'+\frac{1}{2})^2$, where h is Planck's constant, c is the speed of light in vacuum, B_v and D_v are transition dependent rotational constants (taken from Herzberg [23] pp. 106–107, 552) and ω_e and $\omega_e x_e$ are transition dependent vibrational constants (taken from Herzberg [23] pg 552). A Gaussian convolution kernel is used to broaden the simulated spectral lines to match the equipment based line broadening of the experimental spectra. Monte Carlo Markov chains are used for fitting the experimental and simulated data resulting in a range of credible values for T_r. From the distribution of the returned values, a 95 % credibility range for the temperature can be stated. An example fit between the experimental data obtained in *MiniPR* and a simulated spectrum is shown in Fig. 3 for a 30 W, 1.6 Torr argon plasma with 1 % N_2 addition and a pressure gradient of 5000 between the upstream plenum and vacuum chamber. This fit returned a temperature estimate of 1260 K ± 80 K, in agreement with theoretical estimates of 1000–2000 K.

Nanosecond Imaging

Phase-resolved optical-emission spectroscopy (PROES) is a non-invasive diagnostic technique that can be used to investigate space and time-dependent plasma dynamics [24]. For rf plasmas, this can be achieved using a nanosecond-resolution detector that is fitted with spectral filters and an understanding of the key process that result in the population of excited states and subsequent emission [25]. PROES can also be used in conjunction with numerical simulations for accurate benchmarking [26] and the study of sustainment mechanisms [27].

The time-resolved emission as viewed along the central axis of the larger 4 mm-diameter *Pocket Rocket* is shown in Fig. 4. The experimental conditions, apart from the pressure and power described below, are identical as those presented previously [28] and the emission intensity of a single row of pixels is shown with respect to radial distance. Here the camera is fitted with a 488 nm filter (full-width half maximum 10 nm) for observation of the Ar II line, $4p^2D^o - 4s^2P$ at 487.986 nm, the intensity of which is understood to scale with the electron density [7]. For increasing pressure over 1.5–3.25 Torr at 40 W, the formation of an annulus once per rf cycle (80 ns at 12.5 MHz) is observed and this is qualitatively consistent with previous observations of hollow cathode plasma sources [29]. The bright mode shown on Fig. 4a is the mode of interest for thruster applications and the focus of the computer simulations described in Sect. 9.

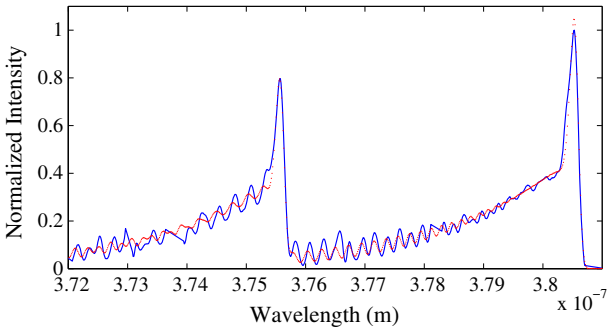

Fig. 3 Example rovibrational band fitting for a 30 W, 1.6 Torr argon discharge with 1 % N_2 added giving a neutral gas temperature estimate of 1260 K. The experimental spectrum is shown as a *blue line*, with the simulated spectrum overlayed with *red dots* (Color figure online)

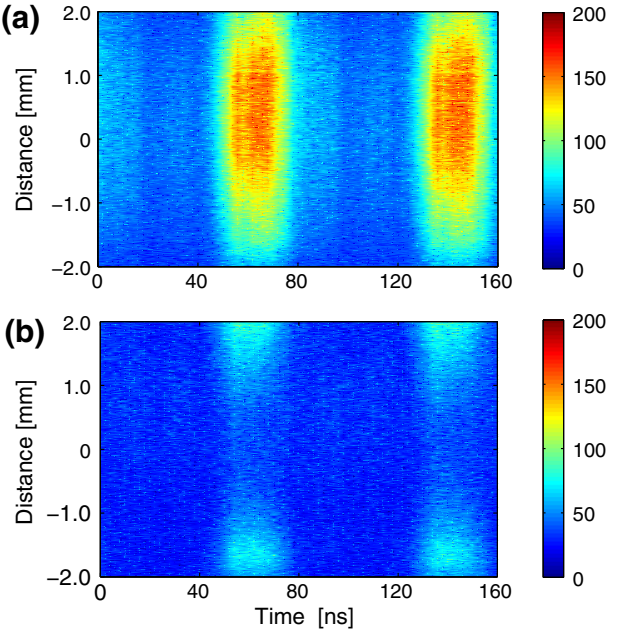

Fig. 4 Variation in the optical-emission intensity, as viewed through the plenum, with respect to radial distance and time during two cycles of the 12.5 MHz rf voltage for a plenum pressure of **a** 1.5 Torr and **b** 3.25 Torr. The intensity of the optical emission is shown by the *colours* and has arbitrary units (Color figure online)

Momentum Diagnostics

Gas pressure profiles along the central axis can be obtained using a Pitot tube as was carried out in a 4 mm-diam system with a similar upstream/downstream pressure ratio of over 200 [30]. This gives some indication of the pressure decrease between the start and end of the plasma cavity and can be combined with CFD simulations (see Sects. 7 and 8). Once confidence is obtained for a certain geometry, the CFD simulation is more than adequate for detailed gas flow calculations. A custom-made thrust balance dedicated to

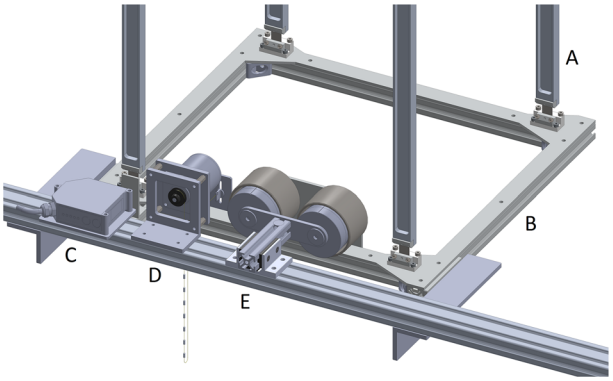

Fig. 5 Schematic of the thrust balance showing main components: **A** pendulum arms, **B** *top open plate*, **C** laser-sensor system, **D** motor driven calibration system and **E** optional voice coil damping system (the thruster is attached to an *open square* mounting suspended to the balance and not shown for clarity)

cold gas and plasma measurements of axial momentum was optimised for low power and small size rf thrusters such as the present prototype based on an earlier design [31]. It is shown on Fig. 5: it consists of four arms (A), a top open plate (B), a laser-sensor system (C), a motor driven calibration system (D) and an optional voice coil damping system (E). The payload is an open square frame (onto which any thruster can be mounted) suspended to part B as described in detail in Ref [32]. There is a locking mechanism which enables the critical test of possible rf or laser drift interference onto the measurement.

Analytical Model

Standard global plasma models in cylindrical geometry [33] can be used to estimate the electron temperature from a particle balance (given a determined neutral gas temperature) and a plasma density from a power balance (given a rf power). This has been shown in reference [7] where the added ceramic insert has been taken into account (there is effectively a voltage divider consisting of the ceramic capacitance and the plasma sheath capacitance). Here the discharge is deliberately made asymmetric so that a self-bias develops on the ceramic insert in direct contact with the 5 mm wide rf annular electrode. In this configuration the plasma potential amplitude and oscillation are minimised and ion-induced secondary electrons emitted by the ceramic walls generate most of the ionisation [9]. Since the gas pressure is of the order of a few Torr, the ionisation is low (less than one percent) and the plasma density is typically a few 10^{12} cm^{-3} for a few tens of Watts.

CFD Simulations: Cold Gas

The Computational Fluid Dynamics Advanced Computational Environment (CFD-ACE+) package is used to validate some basic aspects dealing with gas flow and plasma flow and expansion. Modelling compressible flows in CFD-ACE+ requires the flow and heat transfer simulation modules. The flow module numerically solves the Navier-Stokes equations for the flow velocity and pressure field for a given meshed geometry. As per the finite volume method, the simulation volume is discretised and the continuity equations numerically integrated over each cell. The result is assigned to the cell centre, and interpolated to the cell faces to determine the flux across each cell interface. Mass conservation is implemented, and pressure is calculated using the iterative SIMPLEC algorithm until convergence. Fixed value boundary conditions (e.g. inlets, outlets, isothermal walls) are imposed by setting a source term in a ficticious cell on the external boundary of the volume, while zero-flux boundary conditions (e.g. symmetric boundaries, adiabatic walls) are achieved simply by setting the cell interface coefficients to zero. The heat transfer module keeps track of energy transfers arising from work done on and by the gas during compression and expansion, as well as to impose thermal boundary and initial conditions. Energy conservation is implemented via the total enthalpy equation, and solved similarly as described above.

The *MiniPR* mesh is two-dimensional, and represents the top-half cross section of the physical device. The mesh is divided into five main regions of structured grids, from upstream to downstream (left to right in Fig. 6): plenum, cavity, nozzle, exhaust, and vacuum. Rotating the mesh about the horizontal axis of symmetry (line AM) renders the cylindrical geometry of *MiniPR* and a hemispherical vacuum region. The inlet (line KL) is

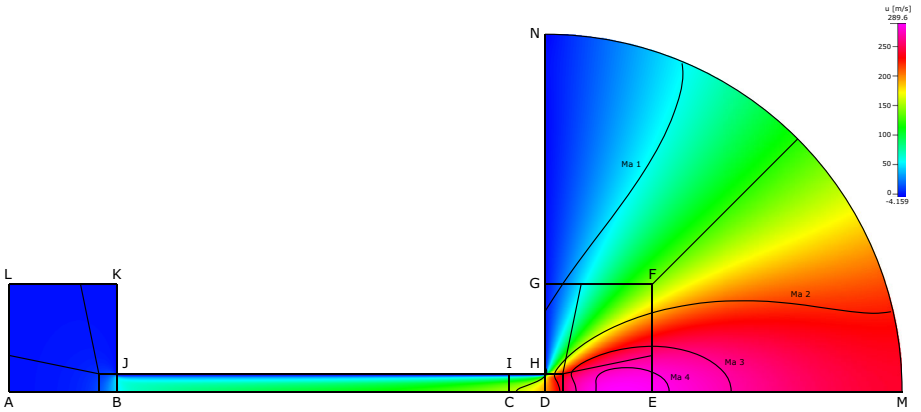

Fig. 6 Axial velocity *colour map* with Mach contours for Xe at a plenum pressure of 7.7 Torr. The Ma 1 contour in the nozzle region shows a parabolic sonic surface where the flow velocity becomes choked, which is expected of a non-slip capillary tube geometry. From *left to right*: plenum (ABKL), cavity (BCIJ), nozzle (CDHI), exhaust (DEFG), and vacuum (EMNGF). Inlet (KL) and outlet (MN) (Color figure online)

defined to be the cylindrical surface of revolution formed by the top boundary of the plenum mesh, and the outlet (line MN) is the hemispherical surface on the far right of the vacuum mesh. Walls (lines AL, KJ, JH and HN) enclose the remaining external boundaries of the mesh.

As much of the gas flow is static in the plenum, it is only necessary for the plenum mesh (area ABKL) to reproduce the region close to the entrance of the cavity where the gas flow begins to accelerate, and the mesh can be coarsened to reduce computation time (e.g. condense a 2×2 grid into 1×1). The cavity mesh (area BCIJ) is square at both ends but transitions smoothly to longer rectangular grids in the middle. This reduces the number of cells and thus computation time, without any loss of accuracy since the cavity flow is one-dimensional. The number of cells across the diameter is the same as in the fine mesh, and is suited for boundary layer flow. In the current *MiniPR* geometry (Fig. 1), the "nozzle" is just the end section of the cylindrical cavity, designated as the region where flow becomes sonic. This nozzle is where most of the important and interesting physics happen, and the behaviour of the nozzle flow dictates the characteristics of the whole flow system both upstream and downstream. Consequently, a high-density mesh is necessary, and a uniform square fine grid is used for the nozzle mesh (area CDHI). The cavity and nozzle meshes are 1:1 scale representations of their physical counterparts in *MiniPR*.

The exhaust mesh (area DEFG) is a mirror image of the plenum mesh, but sufficiently fine to accurately deal with the high dynamic range in flow velocities in that region. The vacuum mesh (area EMNGF) represents the experimental expansion chamber or space, and takes over smoothly from the exhaust mesh. While fluid mechanics are invalid in the vacuum regime, it is a requirement of the simulation to have an outlet boundary condition that brings about vacuum expansion at the nozzle exit. To mitigate unphysical behaviour, the outlet boundary has to be at a sufficient distance away from the important regions of the simulation. A hemispherical outlet boundary is equidistant from the nozzle exit and isotropic, eliminating the directional bias that arises from having boundaries at unequal distances, as well as computational anomalies caused by corners. Also, a hemispherical mesh has fewer cells than a cylindrical mesh of the same radius, and allows the grid to

expand smoothly and uniformly in both radial and polar directions. It is beneficial to coarsen the vacuum mesh for speed; the loss of resolution is unimportant since the results in this region are not used for analysis. In total, there are 69,300 cells in the simulation model presented here.

CFD-ACE+ requires three main categories of input: volume conditions, boundary conditions, and initial conditions. Volume conditions are the properties of the test gas propellant: density, viscosity, specific heat, and thermal conductivity. Boundary conditions are set with the inlet at a chosen fixed plenum pressure and a temperature of 300 K, and the outlet at 0 Torr and 0 K. The walls are no-slip and isothermal at 300 K, with the exception of the vacuum-facing wall which is inviscid. The initial conditions are set individually for each region, starting at the chosen pressure and temperature in the plenum at zero velocity, with decreasing pressure and temperature and increasing velocity in the successive regions. The program offers a means to keep track of residuals and also monitor physical parameters at chosen points in the model. The simulation is left to run until the solution converges to stability and the parameters maintain their final values. The simulation outputs a 2D map of parameters such as velocities, density, pressure, temperature, and mass flow rate, which can be compared to experimental results. This technique is the basis for future direct comparison to experimental cold gas thrust measurements in vacuum as discussed in Sect. 5 and in Ref [32].

It is important to note that CFD-ACE+ is not designed to model vacuum expansion, and the program has not been validated for supersonic flows beyond Mach 2. Despite this, it has been experimentally and theoretically verified that the simulations consistently produce correct results in the necessary regions owing to flow velocity choking. Under choked conditions, the flow behaviour at and upstream of the sonic flow surface is independent of the conditions downstream. For the purposes of these simulations, it does not matter if the gas in the vacuum region was accurately modelled with the appropriate vacuum expansion mechanics or inaccurately with fluid mechanics as it does not affect conditions in the nozzle region and further upstream. The simulations were able to reproduce results in good agreement with the measured pressures and mass flow rates in laboratory experiments, and also successfully replicated the sonic surfaces for various nozzle geometries detailed in [34].

CFD Simulations: Plasma

As an extension to the cold gas fluid simulations described above, the CFD-ACE+ program is capable of modeling capacitively coupled plasma (ccp) discharges, including sheaths, Joule heating, surface reactions and space charge effects. Successful CFD simulations utilizing commercial packages, such as CFD-ACE+, have successfully been performed for weakly ionized and dual frequency CCPs [9, 35, 36].

Here the CFD-ACE+ package is used for a 2D fluid based simulation of the *Pocket Rocket* device. The model used is a the top-half of a 2D cross section, with axisymmetry applied around the central axis to provide a quasi-3D simulation with minimal computing power. The plenum chamber, discharge tube and downstream expansion region are all included in the simulation. It should be noted that the *Pocket Rocket* device modeled here has a 4.2 mm inner discharge tube diameter with a pressure gradient of two between the plenum chamber and downstream expansion region for direct comparison to previous experiments for validation [9]. A complete description of the CFD-ACE+ program and

model in regards to simulations of capacitively coupled plasma (ccp) micro-thrusters can be found in Greig *et al.* [9].

Results of a full ccp CFD simulation include complete flow parameters (velocity, pressure, temperature, etc) as well as electric parameters (potential, charge particle flux, etc) and plasma parameters (plasma density, electron temperature, charged particle mobility etc). These are all provided as complete 2D colour maps over the solution domain. For example, a 2D plot of plasma (ion) density in the *Pocket Rocket* discharge tube is shown in Fig. 7. The input parameters were 240 V peak to peak rf power at 13.56 MHz, a pressure gradient of 2 (inlet and outlet pressures of 1.5 and 0.75, respectively), a secondary electron emission coefficient of 0.1 and four gas phase reactions [9] (elastic, ionization, excitation and stepwise ionization).

The peak in ion density in the centre of the tube, visible in Fig. 7, has been previously noted in experiments by Charles et al. [7]. Charles *et al.* measured ion saturation (I_{sat}) current along the central axis of the 4.2 mm inner diameter *Pocket Rocket* discharge tube using a Langmuir Probe and observed a peak in I_{sat} at the axial midpoint of the tube. As I_{sat} is directly proportional to ion density [37], the ion density therefore peaks at the midpoint of the tube.

A qualitative comparison between ion density from the CFD simulation and I_{sat} previously measured by Charles *et al.* [7] is shown in Fig. 2. The experimental measurements are shown as open circles, with the simulation result shown as a solid black line, and both have been normalized to allow direct comparison. Also shown in Fig. 2 is the normalized CFD simulation result for ion density along the central axis with a pressure gradient of 2000 between the plenum chamber and expansion region (dashed line) for comparison. The remaining simulations parameters are as for the case where the pressure gradient is two.

The experimental ion saturation current and both simulated ion density profiles peak at x = 11 mm, corresponding to the centre of the powered electrode. Downstream of the peak, the experimental results taper off slower than the simulation results due to flow constriction from the Langmuir probe increasing error bars in that region.

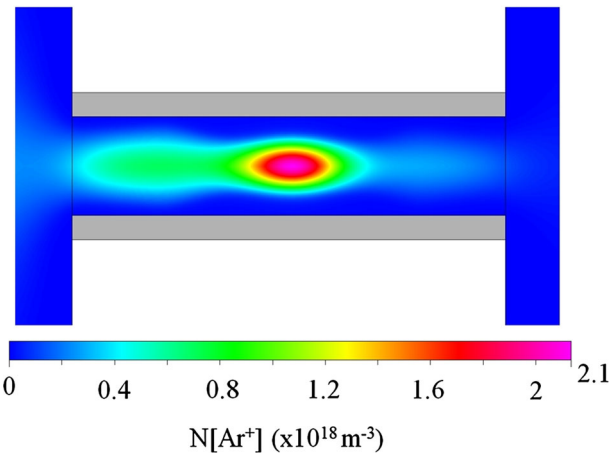

Fig. 7 CFD simulation results for plasma (ion) density in the discharge tube of a 4.2 mm diameter *Pocket Rocket* prototype. The plot has been mirrored around the central thruster axis and cropped to show only the discharge tube (region of interest) for clarity; the input parameters were 240 V peak to peak rf power at 13.56 MHz, a pressure gradient of 2 (inlet and outlet pressures of 1.5 and 0.75, respectively) and a secondary electron emission coefficient of 0.1

Particle in Cell Computer Simulations

A 1D-3v Particle in Cell (PIC) simulation including an axial pressure gradient (1 Torr to 1 mTorr) is developed to focus on the details of the electron and ion energy distributions along the argon plasma jet and get some insight into the energy transfer resulting from ion-neutral collisions using elastic (*ice*) and charge exchange (*icc*) ion-neutral collisions histograms [5]. The PIC code [38, 39] includes elastic, excitation and ionisation electron-neutral collisions and elastic and charge exchange ion-neutral collisions in argon and here the simulation domain is set from x = 0 to x = 0.054 m with 500 grid points to be three times that of the thruster plasma cavity length of 0.018 m (Fig. 1). The plenum cavity is not taken into account and the simulation is bounded by two absorbing walls at x = 0 and x = 0.054 m, respectively.

Since the maximum measured density is localised in the vicinity of the rf annular electrode (x = 0.006–0.011 m) rf 'inductive' heating at 13.56 MHz is applied in both the y and z directions [40, 41] (using an input antenna current density of 5 $A.m^{-1}$ in each direction) from x = 0.006 to 0.011 m to create the generation of a localised plasma in that region. This corresponds to the operation mode with an argon plenum pressure of 1.5 Torr yielding a density peaking on the central axis (Figs. 4a and 2) and displaying characteristics common to an inductive discharge as reported by Dixon et al. [42]: the chosen rf 'inductive' heating method in the PIC most closely resembles these experimental measurements which clearly show that capacitive sheath heating (stochastic) does not play an important role in heating the electrons.

A set gas pressure profile is assumed in the PIC simulation (corresponding to a plenum pressure of 1.6 Torr at x=0 decreasing to a chamber pressure of 0.7 mTorr at x=0.054 m) and the pressure gradient is simulated by a 'random' neutral extracted from a Maxwellian distribution at a fixed temperature T_{gas} (set at 300 K in this study): virtual neutrals are created with given random energy from a Maxwellian to collide with electrons and ions (the neutrals act as an energy sink at a fixed temperature T_{gas} and this is a simplification of the actual experiment). The ion and electron fluxes remain constant along the expansion since there is neutrality and the particle loss only occurs at the two ends of the simulation set as 'absorbing' walls. Typical axial density profiles and electron energy distributions have been previously shown which correlate well with experimental results available in the literature [7].

The PIC simulation can provide statistical results shown on Fig. 5 on the energy transfer between ions and neutral by building elastic (*ice*) and charge exchange (*icc*) ion-neutral collisions histograms (the same principle can be used to monitor electron-neutral energy transfer). Although these two histograms are cumulative and initiated at the start of the simulation, only data representative of the equilibrium state (step 2,000,220 to step 9,399,480 with a time step $\delta t = 10^{-10}$s) is used which corresponds to a total simulated time of 10,000 rf cycles ($\Delta t_{hist} \sim 740$ microseconds). They are built using 100 axial bins from 0 to L, the length of the system, and 200 energy bins from −7.5 to +7.5 eV. Each ion-neutral collision is recorded as follow: the count is incremented in the *ice* or *icc* collision histogram with the axial location of the collisional event tagged to the appropriate axial bin and the corresponding energy transfer tagged to the appropriate energy bin. The energy transfer is referenced to the ion frame (since neutrals are maintained at 300 K) and is calculated using $\delta E_i = E_{i_{after}} - E_{i_{before}}$ where $E_{i_{after}}$ and $E_{i_{before}}$ are the ion energy after and before the collision, respectively ($E = \sqrt{v_x^2 + v_y^2 + v_z^2}$). If the ion looses energy to the

neutral during the collision, $\delta E \leq 0$, and if the ion gains energy from the neutral during the collision, $\delta E \geq 0$.

The analysis also provides the total axial gain ($\delta E \geq 0$) and total axial loss ($\delta E \leq 0$) resulting from all *ice* and *icc* collisions (about 124 million collisions are tagged of which 60 percent are *ice* collisions): the axial gain and loss power respectively correspond to $\sim$(counts $\times \delta E \times q_{factor} \times e)/\Delta t_{hist}$ where e is the elementary charge (energy and power in the simulation are in units of Joule/m^2 and Watt/m^2). The net axial power (gain+loss) is also shown on Fig. 8: it is negative along the entire length of the system, showing that there is a net energy transfer from the ions to the neutrals at all location. This result here is largely underestimated since the neutrals are treated as a thermal sink. It however indicates that there is a very efficient energy transfer as soon as the discharge is in steady-state in agreement with quasi-instantaneous heating from the plasma measured recently [6]. The basic case simulated here closely relates to the 'open system' analytical analysis by Fruchtman [43].

Subsystems and Nano-Satellite Integration

To mitigate the increasing expense of satellites the current trend is moving towards decreased satellite size and the use of Commercial-Off-The-Shelf (COTS) components. A standardised platform is the 10 cm × 10 cm × 10 cm *Cubesat* Unit (1U) which can be expanded to a 6 Unit array. This is opening doors to a wide range of opportunities from technology demonstration, scientific research, communications to education in

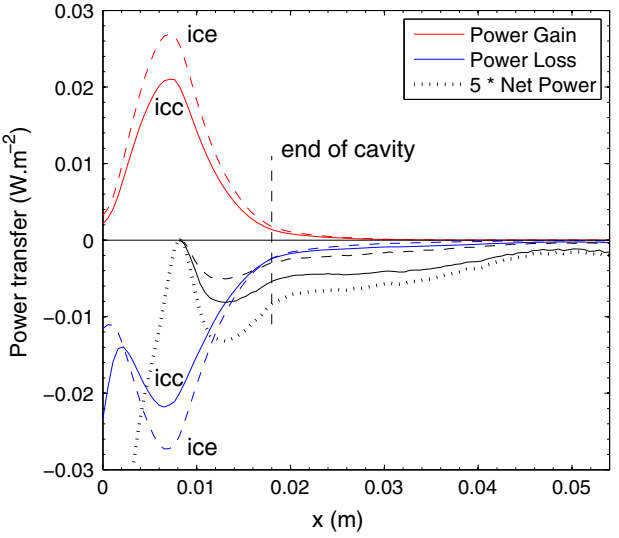

Fig. 8 Results of *ice* (elastic) and *icc* (charge-exchange) ion-neutral collisions histograms cumulated over 10,000 rf cycles (740 microseconds) showing axial profiles of the respective Power Gain (*red lines*: energy transferred from neutrals to ions), Power Loss (*blue lines*: energy transferred from ions to neutrals) and the *ice* (*dashed black line*), *icc* (*solid black line*) and *ice* + *icc* combined (*dotted black line*) Net Power (Gain+Loss); all 3 net powers are multiplied by a factor of 5 for better clarity; end of plasma cavity (*vertical dashed line*) (Color figure online)

multidisciplinary areas. An improved *MiniPR* thruster prototype has now been installed on a thrust balance in the 1 m diameter, 2 m long *Wombat* vacuum chamber equipped with turbo molecular and cryogenic pumping. Thrust has been measured [32] and the results are in agreement with the predictions detailed in Ref [7]. To date there is no available COTS radiofrequency amplifiers space qualified for nano-satellites and much development is still needed prior to achieving a flight demonstrator. Over the past few years, the Australian National University has developed the Advanced Instrumentation Technology Centre which hosts a suite of facilities (the 3 m diameter, 6 m long *Wombat XL* thermal-vacuum chamber, an anaechoic chamber, satellite shakers and a cleanroom) designed to accommodate the complete development process from proof of concept to satellite testing. It also includes a ground station for communication with satellites. Unlike most facilities in the space industry sector this national facility is open to external domestic and international users.

Conclusion

A short review of experimental and computational diagnostics for radiofrequency plasma micro-thrusters has been presented using the *MiniPR* electrothermal radiofrequency plasma thruster prototype. Combining the use of various diagnostics facilitates a more detailed understanding of the basic physics. The application of such a device to space use is very challenging and has necessitated the development of a thrust balance which can now be used as a new type of plasma diagnostic. It is possible to use the Computational Fluid Dynamics Advanced Computational Environment (CFD-ACE+) package to validate some basic aspects of the plasma discharge (gas flow, plasma density, plasma potential, self bias). Therefore future studies with the addition of geometric, chemical and thermal effects can be envisaged to accelerate the thruster development. More elaborate methods such as a Particle In Cell simulations and nanosecond optical emission based spectroscopy can be used to address mode fundamental unresolved questions related to rf power coupling into the plasma and detailed spatio-temporal collisional processes. Plasma experiments in space may also be envisaged in the long term.

Acknowledgments This research was funded by the Australian Research Council Discovery Projects DP 1096653 and DP140100571 and by the Australian Space Research Program ('Australian Plasma Thruster' project with thanks to Jai Vennik for Fig. 5). The original Particle In Cell code written by Dr. Trevor Lafleur was rewritten and modified for the present study by Rhys Hawkins at ANU Supercomputer Facility as part of the ARC DP1096653 project. This project also partially supported the visit by Prof. Timo Gans and Dr. Deborah O'Connor (fast imaging testing campaign of *Pocket Rocket* at the ANU Space Plasma, Power and Propulsion Laboratory in January/February 2012) and we thank both collaborators for useful discussions. Sects. 4 and 8 were written by Amelia Greig and Sect. 7 was written by Teck Seng Ho.

References

1. Goebel DM, Katz I (2008) Fundamentals of electric propulsion: ion and Hall thrusters. Wiley, London
2. Sankaran RM, Giapis KP (2001) Maskless etching of silicon using patterned microdischarges. Appl Phys Lett 79:593–595
3. Cao Z, Walsh JL, Kong MG (2009) Atmospheric plasma jet array in parallel electric and gas flow fields for three-dimensional surface treatment. Appl Phys Lett 94:021501
4. Charles C, Boswell RW, Bish A (2014) Low-weight fixed ceramic capacitor impedance matching system for an electrothermal plasma microthruster. J Propuls Power 30(4):1117–1121

5. Charles C, Hawkins R, Boswell RW (2015) Particle in cell simulation of a radiofrequency plasma jet expanding in vacuum. Appl Phys Lett 106:093502
6. Greig A, Charles C, Paulin N, Boswell RW (2014) Volume and surface propellant heating in an electrothermal radio-frequency plasma micro-thruster. Appl Phys Lett 105:054102
7. Charles C, Boswell RW (2012) Measurement and modeling of a radiofrequency micro-thruster. Plasma Sources Sci Technol 21:022002
8. Dixon S, Charles C, Boswell R (2013) Spatial evolution of eepfs in a millimetre scale radio frequency argon plume. J Phys D Appl Phys 46(36):365202
9. Greig A, Charles C, Boswell RW (2015) Simulation of main plasma parameters of a cylindrical asymmetric capacitively coupled plasma micro-thruster using computational fluid dynamics. Front Phys 2(80):1–9
10. Gottscho RA, Donnelly VM (1984) Optical emission actinometry and spectral line shapes in rf glow discharges. J Appl Phys 56(2):245–250
11. Phillips DM (1976) Determination of gas temperature from unresolved bands in the spectrum from a nitrogen discharge. J Phys D Appl Phys 9(3):507
12. Bruggeman PJ, Sadeghi N, Schram DC, Linss V (2014) Gas temperature determination from rotational lines in non-equilibrium plasmas: a review. Plasma Sources Sci Technol 23(2):023001
13. Poirier J-S, Brub P-M, Muoz J, Margot J, Stafford L, Chaker M (2011) On the validity of neutral gas temperature by N2 rovibrational spectroscopy in low-pressure inductively coupled plasmas. Plasma Sources Sci Technol 20(3):035016
14. Bak MS, Kim W, Cappelli MA (2011) On the quenching of excited electronic states of molecular nitrogen in nanosecond pulsed discharges in atmospheric pressure air. Appl Phys Lett 98(1):011502
15. Bai Bo, Sawin Herbert H, Cruden Brett A (2006) Neutral gas temperature measurements of high-power-density fluorocarbon plasmas by fitting swan bands of c2 molecules. J Appl Phys 99(1):013308
16. Moon SY, Choe W (2003) A comparative study of rotational temperatures using diatomic OH, O2 and N2+ molecular spectra emitted from atmospheric plasmas. Spectrochim Acta Part B At Spectrosc 58(2):249–257
17. Huang X-J, Xin Y, Yang L, Yuan Q-H (2008) Spectroscopic study on rotational and vibrational temperature of N2 and N2+ in dual-frequency capacitively coupled plasma. Phys Plasmas 15:113504
18. Takahashi T, Takao Y, Eriguchi K, Ono K (2009) Numerical and experimental study of microwave-excited microplasma and micronozzle flow for a microplasma thruster. Phys Plasmas (1994-present) 16:083505
19. Fishburne ES (1967) Transfer of electronic energy between a metastable argon atom and a nitrogen molecule. J Chem Phys 47(1):58–63
20. Greig A, Charles C, Hawkins R, Boswell RW (2013) Direct measurement of neutral gas heating in a radio-frequency electrothermal plasma micro-thruster. Appl Phys Lett 103:074101
21. Dunham JL (1932) The energy levels of a rotating vibrator. Phys Rev 41:721–731
22. Zare RN, Larsson EO, Berg RA (1965) Franck-condon factors for electronic band systems of molecular nitrogen. J Mol Spectrosc 15(2):117–139
23. Herzberg G, Huber KP (1945) Molecular spectra and molecular structure. Prentice-Hall, Inc, Englewood Cliffs
24. Gans T, O'Connell D, Schulz-von der Gathen V, Waskoenig J (2010) The challenge of revealing and tailoring the dynamics of radio-frequency plasmas. Plasma Sources Sci Technol 19(3):034010
25. Boffard JB, Lin CC, De Joseph CA Jr (2004) Application of excitation cross sections to optical plasma diagnostics. J Phys D Appl Phys 37(12):R143
26. Niemi K, Reuter S, Graham LM, Waskoenig J, Knake N, Schulz-von der Gathen V, Gans T (2010) Diagnostic based modelling of radio-frequency driven atmospheric pressure plasmas. J Phys D Appl Phys 43(12):124006
27. Bruneau B, Gans T, O'Connell D, Greb A, Johnson EV, Booth J-P (2015) Strong ionization asymmetry in a geometrically symmetric radio frequency capacitively coupled plasma induced by sawtooth voltage waveforms. Phys Rev Lett 114:125002
28. Charles C, Dedrick J, Boswell RW, O'Connell D, Gans T (2013) Nanosecond optical imaging spectroscopy of an electrothermal radiofrequency plasma thruster plume. Appl Phys Lett 103(12):124103
29. Lazzaroni C, Chabert P, Rousseau A, Sadeghi N (2010) The excitation structure in a micro-hollow cathode discharge in the normal regime at medium argon pressure. J Phys D Appl Phys 43(12):124008
30. Dixon S, Charles C, Boswell R, Cox W, Holland J, Gottscho R (2013) Interactions between arrayed hollow cathodes. J Phys D Appl Phys 46(14):145204
31. Lafleur T, Takahashi K, Charles C, Boswell RW (2011) Direct thrust measurements and modelling of a radio-frequency expanding plasma thruster. Phys Plasmas 18:080701

32. Charles C, Boswell RW, Bish A, Khayms V, Scholz E (2015) Direct measurement of axial momentum imparted by an electrothermal radiofrequency plasma micro-thruster. Submitted to Plasma Sources Sci Technol
33. Lieberman MA, Lichtenberg AJ (2005) Principles of plasma discharges and plasma processing. Wiley, London
34. Murphy HR, Miller DR (1984) Effects of nozzle geometry on kinetics in free-jet expansions. J Phys Chem 88(20):4474–4478
35. Kolobov VI (2003) Fokker–planck modeling of electron kinetics in plasmas and semiconductors. Comput Mater Sci 28(2):302–320
36. Lu Y, Yan D, Chen Y (2009) 2-D fluid simulation of dual-frequency capacitively coupled plasma. J Hydrodyn Ser B 21(6):814–819
37. Sheridan TE (2000) How big is a small langmuir probe? Phys Plasmas 7(7):3084–3088
38. Lafleur T, Boswell RW, Booth JP (2012) Enhanced sheath heating in capacitively coupled discharges due to non-sinusoidal voltage waveforms. Appl Phys Lett 100(19):194101
39. Lafleur T, Boswell RW (2012) Particle-in-cell simulations of hollow cathode enhanced capacitively coupled radio frequency discharges. Phys Plasmas 19(2):023508
40. Baalrud SD, Lafleur T, Boswell RW, Charles C (2011) Particle-in-cell simulations of a current-free double layer. Phys Plasmas 18:063502
41. Meige A, Boswell RW, Charles C, Turner MM (2005) One-dimensional particle-in-cell simulation of a current-free double layer in an expanding plasma. Phys Plasmas 12:052317
42. Dixon S, Charles C, Dedrick J, Gans T, O'Connell D, Boswell R (2014) Observations of a mode transition in a hydrogen hollow cathode discharge using phase resolved optical emission spectroscopy. Appl Phys Lett 105:014104
43. Fruchtman A (2008) Energizing and depletion of neutrals by a collisional plasma. Plasma Sources Sci Technol 17(2):024016